

Nanoscale

Accepted Manuscript



This is an *Accepted Manuscript*, which has been through the Royal Society of Chemistry peer review process and has been accepted for publication.

Accepted Manuscripts are published online shortly after acceptance, before technical editing, formatting and proof reading. Using this free service, authors can make their results available to the community, in citable form, before we publish the edited article. We will replace this *Accepted Manuscript* with the edited and formatted *Advance Article* as soon as it is available.

You can find more information about *Accepted Manuscripts* in the [Information for Authors](#).

Please note that technical editing may introduce minor changes to the text and/or graphics, which may alter content. The journal's standard [Terms & Conditions](#) and the [Ethical guidelines](#) still apply. In no event shall the Royal Society of Chemistry be held responsible for any errors or omissions in this *Accepted Manuscript* or any consequences arising from the use of any information it contains.

ARTICLE

Sandwich-structured nanohybrid paper based on controllable growth of nanostructured MnO₂ on ionic liquid functionalized graphene paper as flexible supercapacitor electrode

Cite this: DOI: 10.1039/x0xx00000x

Received 00th January 2012,

Accepted 00th January 2012

DOI: 10.1039/x0xx00000x

www.rsc.org/

Yimin Sun,^{*a,b} Zheng Fang,^b Chenxu Wang,^b K. R. Rakhitha Malinga Ariyawansa,^b Aijun Zhou^a and Hongwei Duan^{*b}

Sandwich-structured flexible supercapacitor electrode has been developed based on MnO₂ nanonests (MNNs) modified ionic liquid (IL) functionalized graphene paper (GP), which is fabricated by functionalizing graphene nanosheets with amine-terminated IL (i.e., 1-(3-aminopropyl)-3-methylimidazolium bromide) to form freestanding IL functionalized GP (IL-GP), and then modifying IL-GP with unique MNNs structure via a controllable template-free ultrasonic-electrodeposition. The as-obtained MNNs modified IL-GP (MNN/IL-GP) inherits the excellent pseudocapacity of metal oxide, the high conductivity and electric double layer charging/discharging of IL-graphene composite, and therefore shows an enhanced supercapacitor performance. The maximum specific capacitance of 411 F g⁻¹ can be achieved by chronopotentiometry at a current density of 1 A g⁻¹. Meanwhile, the MNN/IL-GP electrode exhibits excellent rate capability and cycling stability, its specific capacitance preserves 70% as the current densities increase from 1 to 20 A g⁻¹ and 85% at a current density of 10 A g⁻¹ after 10000 cycles. More importantly, the MNN/IL-GP displays distinguished mechanical stability and flexibility for device packaging, although its thickness is merely 8 μm. These features collectively demonstrate the potential of MNN/IL-GP as a high-performance paper electrode for flexible and lightweight and highly efficient electrochemical capacitor applications.

Introduction

Flexible, lightweight and highly efficient energy supercapacitor (SC) with large power density, moderate energy density, good operational safety and long cycling life are highly desirable as an attractive power source for many demanding systems.¹⁻⁵ The design of flexible SC devices necessitate the development of flexible electrode with favourable mechanical and capacitive properties. Carbon-based paper-like materials, such as carbon cloth and carbon nanofiber paper that possess large surface area and high electric double-layer capacitance are primarily used as active free-standing and flexible electrode materials for flexible energy storage application.⁶⁻¹¹ However, the relatively high weight fraction, the elaborate and complex procedures and high-cost limit their wide spectrum of applications in energy system. Therefore, it is still a great challenge to fabricate ultra-thin paper electrode with favourable mechanical strength and low cost that can be scaled up for widespread commercialization.

Graphene has emerged as a new class of two-dimensional carbon nanostructure, which holds great promise in electrochemical applications because of the unprecedented combination of high electrical and thermal conductivities, good transparency, great mechanical strength, inherent flexibility and huge specific surface area.^{12,13} More importantly, graphene can be produced in large scale

at relatively low cost. Recent reports including ours have shown that graphene or graphene oxide (GO) sheets can indeed be assembled into ultra-thin graphene paper (GP) structure with excellent flexibility, mechanical stiffness and exceptional electrical conductivity,¹⁴⁻²¹ which make them promising as high performance flexible electrode for SC application. Nevertheless, the surface area of GP is usually much lower than the theoretical values because of the restacking and aggregation of graphene nanosheets during the formation of freestanding paper structure,^{22,23} which is detrimental for the electrolyte to penetrate into the inner layer of GP. In addition, the SC systems based on carbon materials currently suffer from a major limitation of low energy density,²⁴ Increasing evidences have shown that the development of hybrid SC electrode by combining the electric double-layer capacitance and pseudocapacitance is a possible solution.²⁵ The optimal electrode materials for SC applications are expected to consist of multiple components such as conductive carbon materials with high specific surface area and double-layer capacitance, and redox active materials of conductive polymers or transition metal oxides providing pseudocapacitance. Our recent success in preparing freestanding Mn₃O₄ nanoparticles modified GP by intercalated Mn₃O₄ nanoparticles between the graphene layers has been proved to be an effective way to fabricate multilayered nanohybrid GP, which exhibited excellent mechanical stability, greatly improved active surface areas, and enhanced ion transportation in comparison with the pristine GP.²⁶

In this work, we have adopted two strategies to improve the supercapacitive properties of GP materials by firstly functionalizing graphene nanosheet with amine-terminated ionic liquid (IL) to form free-standing nanohybrid IL-GP, and then modifying IL-GP with unique MnO₂ nanonests (MNNs) structure *via* a controllable template-free ultrasonic-electrodeposition method. This method leads to the formation of sandwich-structured nanohybrid paper with better structural integration of IL and MNNs with GP. ILs are normally organic salts with properties of being easily adjusted by changing one of the ions. They feature moderately intrinsic conductivity, nonvolatility, wide solubility range, high decomposition temperatures, nontoxicity, and environmental compatibility,²⁷ and therefore are widely used as electrolytes in advanced SC systems with improved energy and power densities, operation safety, and lifetime.²⁸ The application of IL-graphene nanocomposition as active materials for SC electrode also holds great promise.^{24,29,30} A few of works have demonstrated that the IL-graphene nanocomposition can achieve the capability of being well dispersed and stabilized in various solvents by covalently functionalizing graphene with ILs (i.e., 1-(3-aminopropyl)-3-methylimidazolium bromide).³¹ By modifying surface of graphene with IL polymers poly(1-vinyl-3-ethylimidazolium) bis(trifluoromethylsulfonyl) amide *via* electrostatic and cation- π interaction between graphene and IL units, the poly IL modified graphene nanocomposite provided enhanced compatibility with the IL electrolyte, thereby increasing the effective electrode surface area accessible to electrolyte ions.³² In our work, the amine-terminated ILs (i.e., 1-(3-aminopropyl)-3-methylimidazolium bromide) have been covalently attached on the graphene nanosheets, which not only act as “spacer” to prevent graphene aggregation from forming compact paper structure, but also increase the capacitive activity of the resulting paper electrode. The as-obtained IL-GP is expected to provide highly conductive channels to effectively transport electrolyte and serve as an electrochemical active substrates for immobilizing the pseudocapacitive nanostructure to process into freestanding and flexible electrodes.³³

Among a diverse range of pseudocapacitive materials, MnO₂ is considered as an ideal electrode material owing to their high energy density and large charge transfer-reaction pseudocapacitance.³⁴ In our work, the MnO₂ materials with different nanostructure have been synthesized by well controllable template-free ultrasonic-electrodeposition under different conditions, which provides insight on how the overall performance is related to the structural parameters such as the degree of surface coverage and the morphology of the nanostructures. Electrodeposition is a green, low-cost, convenient and effective technique for producing nanostructure metal/metal oxide materials, allowing for controlling the film surface morphology, grain size, chemical state, and thickness by adjusting deposition parameters such as potential, current density, bath composition, and temperature.³⁵⁻³⁸ Our results show that the MNN material exhibits improved supercapacitive properties over other nanostructured MnO₂ materials such as MnO₂ nanomesh (MNM), MnO₂ framework (MFW) and MnO₂ nanoparticles (MNPs), owing to its unique structure that reduces diffusion length over which electrolyte ions must transfer during the charge/discharge process and improves electrochemical utilization of MnO₂. Taken together, the obtained multilayered nanohybrid paper electrode is expected to inherit the unique pseudocapacity of metal oxide, the high conductivity and electric double layer charging/discharging of IL-graphene composite, and the distinguished mechanical flexibility, making it a promising electrode material for advanced flexible and lightweight energy storage devices.

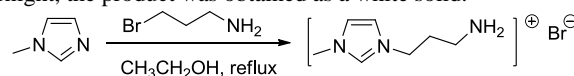
Experimental section

Preparation of graphene nanosheets

GONs was firstly synthesized from graphite powder based on modified Hummer's method.³⁹ The exfoliation of GONs was achieved by ultrasonication of the dispersion for 2 h. GNs were prepared by adding 35% hydrazine aqueous solution into the as-obtained GONs suspension under stirring, and then heated at 95 °C for 1 h. The GONs and GNs were washed with distilled water and dried under vacuum.

Preparation of amino-terminated ionic liquid

Amino-terminated ionic liquid (IL) was prepared according to the literatures, as illustrated in Scheme 1.^{31,40} Equal mole of 3-bromopropylamine hydrobromide and 1-methylimidazole were first dissolved in ethanol. After refluxing under nitrogen for 24 h, the solution turned to be turbid. Then ethanol was evaporated in vacuo, and the crude product was recrystallized with a mixture solution of ethanol and ethyl acetate. After drying under vacuum at 60 °C overnight, the product was obtained as a white solid.



Scheme 1. The synthesis route of amino-terminated ionic liquid 1-(3-aminopropyl)-3-methylimidazolium bromide.

Preparation of amino-terminated ionic liquid functionalized graphene nanosheets

Amino-terminated ionic liquid functionalized GNs (IL-GNs) were synthesized by an epoxide ring-opening reaction between amino-terminated IL 1-(3-aminopropyl)-3-methylimidazolium bromide and GO catalyzed by KOH.⁴⁰ In the typical procedure, excess amount of IL was firstly added into GO dispersion, and the transparent solution turned to be turbid due to the salt effect of the GO sheets. Then KOH was added into the above mixture solution. After ultrasonication, the turbid mixture was transformed to the original transparent status. The solution was vigorously stirred at 90 °C for 24 h. The resulting IL-GNs were centrifuged and washed with ethanol, and redispersed in water.

Preparation of different nanohybrid papers

IL-GP and GP were synthesized by filtration of and IL-GNs and GNs suspensions through a cellulose acetate membrane (0.2 μ m pore size, 85 mm diameter, Whatman) followed by vacuum drying at 80 °C, and then were cut into pieces (dimensions: 30 mm \times 10 mm). Different nanostructured MnO₂ were *in situ* electrodeposited onto the IL-GP and GP from its precursor solution containing 0.1 M Na₂SO₄ and 0.1 Mn(CH₃COO)₂. During the potentiostatic deposition, the solution was irradiated with ultrasonic wave. The ultrasonic intensity and frequency are fixed at 1.5 W cm⁻² and 30 kHz, respectively. For the electrodeposition of MNNs and MNMs, potentiodynamic electrodeposition mode was carried out between the potential limits of +1.4 and -1.5 V with different scan rates and cycle numbers. And for the electrodeposition of MNPs and MFWs, potentiostatic and galvanostatic electrodeposition modes were carried out by applying a deposited potential of +0.6 V and a current density of 0.5 mA cm⁻², respectively. Electrodeposition process was performed at room temperature without any stirring or inert-gas bubbling. After depositing, the electrodes were rinsed with distilled water and dried. The weight of the GP, IL-GP, MNN/GP, MNN/IL-GP, MNM/IL-GP, MFW/IL-GP and MNP/IL-GP were determined by using a high precision microbalance.

Characterization

Atomic force microscopy (AFM) observation was carried out using a MFP3D microscope (Asylum Research) with a silicon cantilever operating in tapping mode. The samples for AFM characterization were spin-coated on silicon wafer with a 300 nm SiO₂ top layer. Scanning electron microscope (SEM) image was obtained using JEOL field-emission scanning electron microscope (JSM-6700F), equipped to perform elemental chemical analysis by energy dispersive X-ray spectroscopy (EDX). Fourier transform infrared (FT-IR) spectra were obtained on a Perkin Elmer Spectrum One Spectrometer. Zeta potential of GONs and IL-GNs suspension in neutral aqueous solutions was measured at room temperature on ZetaPALS Zeta Potential Analyzer (Brookhaven Instruments Corporation). X-ray diffraction (XRD) patterns were collected with a Bruker AXS D8 X-ray diffractometer equipped with monochromatized Cu K α radiation ($\lambda = 1.54056 \text{ \AA}$, 40 kV and 20 mA). X-ray photoelectron spectroscopy (XPS) measurements were performed on a Kratos-Axis spectrometer with monochromatic Al K α (1486.71 eV) X-ray radiation (15 kV and 10 mA) and hemispherical electron energy analyzer. The tensile behaviors of the paper samples were measured using an Instron 8848 Microforce Tester at a loading rate of 2 mm min⁻¹ with a gauge length of 10 mm.

Electrochemical Measurement

Electrodeposition, electrochemical impedance spectroscopy (EIS), cyclic voltammetric (CV) and chronopotentiometric experiments were performed with a CHI 660 D electrochemical workstation (CH Instruments Inc.). A conventional three-electrode system was adopted. The working electrodes were the paper electrodes, and the counter and reference electrodes were Pt foil and saturated calomel electrode (SCE), respectively. The distance between electrodes was kept at 0.5 cm in all experiments. A 1.0 M Na₂SO₄ solution served as electrolyte at room temperature. Cyclic voltammetry (CV) experiments were performed at various scan rates of 2, 5, 10, 20, 50, 100 and 200 mV s⁻¹. Galvanostatic (GV) charge/discharge curves were obtained at various current densities of 1, 2, 5, 10 and 20 A g⁻¹ to evaluate the specific capacitance (C_s). The C_s of different nanohybrid paper electrodes was calculated from the equation of $C_s = I\Delta t/m\Delta V$, where I is the discharge current, Δt is the discharge time, m is the total mass of freestanding paper measured by high-precision microbalance, and ΔV is the voltage drop upon discharge.

Results and discussion

Preparation and Characterization of Sandwich-structured Nanohybrid Paper Electrode

As illustrated in Fig. 1, the procedure for designing sandwich-structured nanohybrid paper involves three key steps. First, single-layered graphene oxide nanosheets (GONs) prepared by Hummer's method³⁹ were chemically modified by amine-terminated IL (i.e., 1-(3-aminopropyl)-3-methylimidazolium bromide) to prepare IL functionalized graphene nanosheets (GNs) through a nucleophilic ring-opening reaction between the epoxy groups of GONs and the amine groups of IL.^{31, 40, 41} A distinct color change of the aqueous GONs solution from brown to black is visible during this process. The introduction of charge and widely soluble IL units to graphene plane leads to the formation of homogeneous GNs suspension with long-term stability. Second, the IL functionalized GNs (IL-GNs) are assembled into freestanding IL-GP by filtration. The as-obtained IL-GP is bendable and black in color, with a slight metal luster on both sides. The low magnification SEM image reveals that the IL-GP has a uniform thickness of $\sim 8 \mu\text{m}$ throughout its entire cross-section. For SC application, the functionalization of graphene with

IL to fabricate IL-GP offers two advantages: (i) to prevent graphene aggregation and restacking from forming paper structure by the electrostatic repulsion and steric hindrance between the grafting IL groups on the graphene in order to increase the specific area of the SC electrode, and (ii) to give rise to the capability of IL-GP being well wetted by electrolyte. Third, nanostructured MnO₂ with optimal architecture of 3D interpenetrating network (i.e., MNNs) are *in situ* electrodeposited on freestanding IL-GP with ultrasonic assistance to form nanohybrid MNN modified IL-GP (MNN/IL-GP).

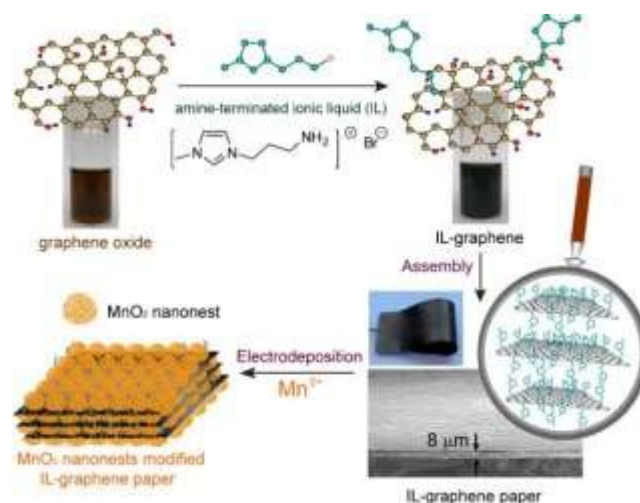


Fig. 1 Illustration of the preparation of sandwich-structured nanohybrid paper.

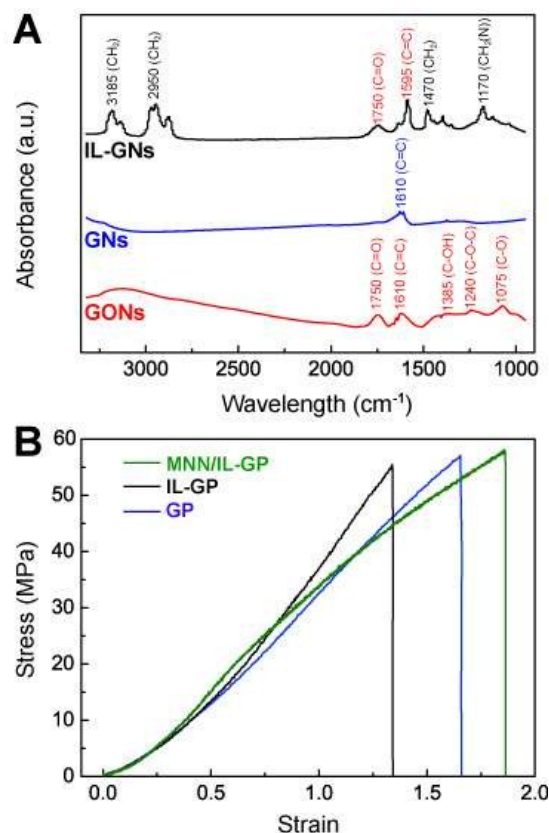


Fig. 2 (A) FT-IR spectroscopy of IL-GNs, GNs and GONs samples. (B) Stress-strain curve of the MNN/IL-GP, GP and IL-GP samples (from right to left).

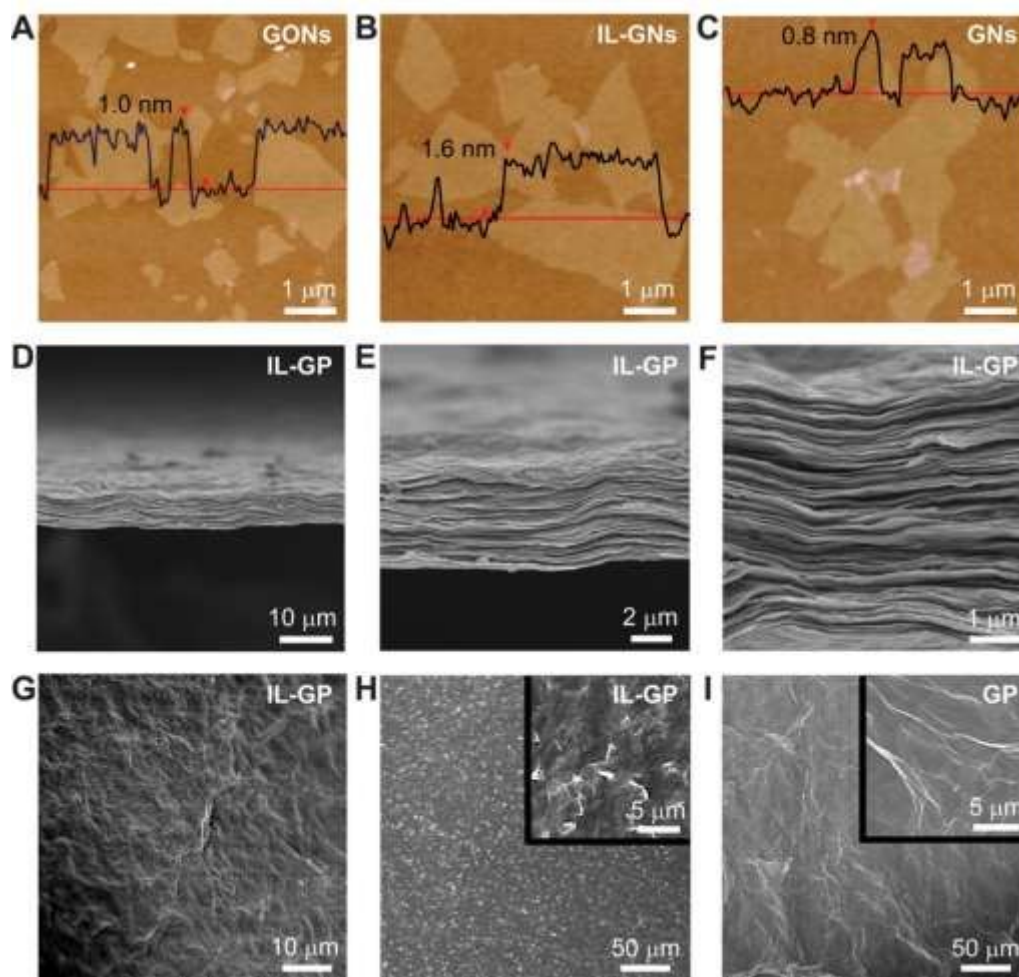


Fig. 3 AFM micrographs of (A) GONs, (B) IL-GNs and (C) GNs. SEM micrographs of (D-F) cross-sectional view of IL-GP with different magnification SEM micrographs of (G) oblique view and (H) top view of IL-GP. SEM micrographs of (I) top view of GP.

FT-IR spectroscopy was used to confirm the successful attachment of amine-terminated IL to GONs and examine the reduction degree of GONs. As presented in Fig. 2A, the spectrum of GONs shows the presence of C–O (ν (epoxy or alkoxy)) at 1075 cm^{-1} , C–O–C (ν (epoxy symmetrical ring deformation vibration)) at 1240 cm^{-1} , C–OH (ν (carboxyl)) at 1385 cm^{-1} , C=C at 1610 cm^{-1} , and C=O in carboxylic acid and carbonyl moieties (ν (carbonyl)) at 1750 cm^{-1} . After chemically reduced by hydrazine, the adsorption bands of oxygen functionalities (i.e., C–O at 1075 cm^{-1} , C–O–C at 1240 cm^{-1} , C–OH at 1385 cm^{-1} and C=O at 1750 cm^{-1}) disappear, only the peak of C=C at 1610 cm^{-1} remains, indicating that most oxygen functionalities have been removed by hydrazine. Similar results have also been obtained for IL-GNs, which shows that most oxygen functionalities disappear, only the peaks of C=C at 1610 cm^{-1} and C=O at 1750 cm^{-1} preserve. Additionally, CH₃–N stretching vibration, CH₂–N stretching vibration, the C–H stretching vibration and ring in plane asymmetric stretching appear at 1170 cm^{-1} , 1470 cm^{-1} , 2950 cm^{-1} and 3185 cm^{-1} . The frequencies of ring C–H stretching vibration, C–N stretching vibration, and ring in plane asymmetric stretching are sensitive to the electronic density of imidazolium ring. This demonstrates that the IL chains have been grafted onto the surface of GNs through a nucleophilic ring-opening

reaction between the epoxy groups of GO and the amine groups of IL 1-(3-aminopropyl)-3-methylimidazolium bromide.⁴²

The filtration of the aqueous IL-GNs dispersion leads to the formation of freestanding IL-GP with excellent mechanical properties and tailored scale in both size and thickness. For comparison, the unfunctionalized GNs are also assembled into GP under the same procedure. Fig. 2B shows the stress-strain curves of the resultant IL-GP and GP samples, both of which exhibit straightening behaviour at the beginning, followed by roughly linear (i.e., elastic) behaviour. The detailed results of the tensile test show that IL-GP has a relative high tensile strength of 55.35 MPa and a strain of 1.34%. These are to some extent lower than those of GP (tensile strength of 57.03 MPa and strain of 1.66%). The worse tensile strength and ductility of IL-GP should be attributed to the electrostatic repulsion and steric hindrance by introducing IL units on the GONs, causing the weaker interlayer interaction of the resultant IL-GP. It is noteworthy that the further electrodeposition of MNN leads to the increase of the tensile strength and strain of MNN/IL-GP, which rise to 57.63 MPa and 1.86%, respectively. The enhancement of the strength might be due to the penetration of MNNs into the internal IL-GP, which reduces the porosity and improves the tensile property of IL-GP.

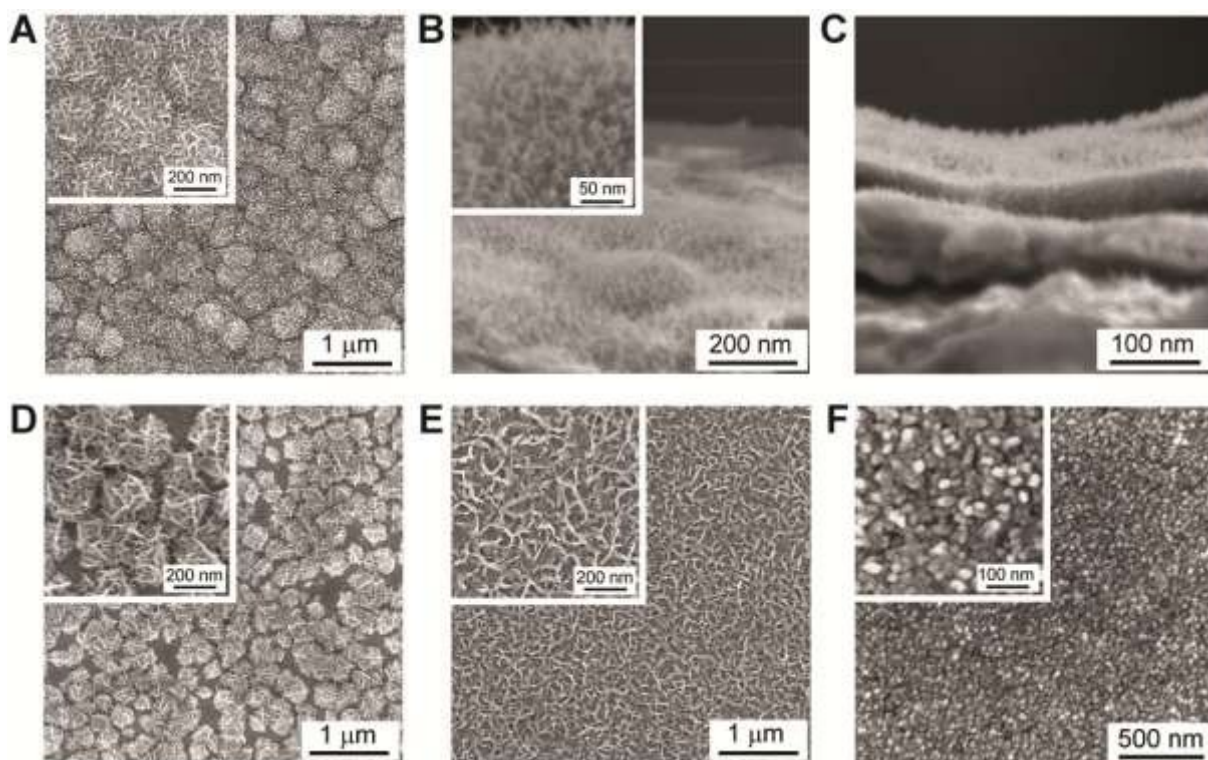


Fig. 4 SEM of (A) top view, (B) oblique view and (C) cross-sectional view of MNN/IL-GP. SEM of top view of (D) MNM/IL-GP, (E) MFW/IL-GP and (F) MNP/IL-GP.

Fig. 3A, 3B and 3C display the AFM images of GONs, IL-GNs and GNs, respectively. The average thickness for IL-GNs is ca. 1.6 nm, much greater than that of exfoliated GONs (1.0 nm) and unfunctionalized GNs (0.8 nm). This is due to the presence of IL chains grafted onto both graphene nanosheet sides, as well as the electrostatic repulsion between the IL-GNs. The value of the zeta potential from the GO suspension is -6.5 mV due to the negatively charged surface of the GO platelets. In contrast, the introduction of the positively charged cations in IL onto the GONs by the through epoxide ring-opening reaction results in the reversal of zeta potential with a value of 3.7 mV. The SEM images of Fig. 3D and 3E reveal that the fracture edges of IL-GP have well-regulated layer-by-layer structure throughout its whole cross section, with a uniform thickness of $\sim 8 \mu\text{m}$. And the void spaces are visible along the fracture edge (Fig. 3F). Furthermore, the oblique and top views of SEM observations show that the surface of IL-GP is quite bumpy (Fig. 3G) and full of protuberances (Fig. 3H). The bulging parts have a typical dimension of several hundred nanometers (Fig. 3H inset). Nevertheless, the GP sample prepared under the same procedure displays the characteristic wrinkle conformation and its surface is quite smooth because of the restacking of GNs during the formation of paper structure (Fig. 3I), resulting in the possible decrease of the effective surface area and lower specific capacitance of GP.

The IL-GP with large effective surface area serves not only as electroactive material that enable effective electrolyte transport and active-site accessibility, but also as an ideal conductive scaffold for *in situ* electrodeposition of MnO_2 nanomaterials, which enables the uniform coating of MnO_2 nanostructures on the entire surfaces of IL-GP samples. Since the morphology and surface area of electrode materials have a profound effect on the overall performance of the electrochemical capacitors, different deposition modes are adopted to obtain MnO_2 nanomaterials with well controllable morphologies. Fig. 4 shows SEM images of top view of different nanostructured

MnO_2 on IL-GP. The MnO_2 film growing on IL-GP by potentiodynamic ultrasonic-electrodeposition modes exhibits the formation of 3D network of MnO_2 nanowire with a typical diameter of less than 10 nm and an average length of 100–200 nm. At the suitable deposition sweep rate of 100 mV s^{-1} and sweep segment of 20 cycles, the as-formed nanowires are interweaved into nanonest microstructure (Fig. 4A and 4B), leading to high porosity of the architecture. Of note is that the *in situ* electrodeposition results in the formation of MnO_2 not only in the exterior part but also in the inner part of IL-GP (Fig. 4C), which are expected to provide large accessible surface area that enable effective electrolyte ion transport during SC operations. When the sweep rate declines to 50 mV s^{-1} and sweep segment decreases to 10 cycles, the deposited nanowires become sparse (Fig. 4D), mainly due to the longer time interval between every deposition segments.⁴³ In this case, the configuration of intertwined nanowires is MnO_2 nanomesh (MNM). For comparison, the MnO_2 film obtained by galvanostatic mode with ultrasonic assistance shows the formation of numerous MnO_2 nanoflakes, which arrange into typical mesoporous MnO_2 framework (MFW) architecture with average mesopores size of $\sim 100 \text{ nm}$ (Fig. 4E). And the potentiostatic mode leads to the formation of homogeneous tiny MnO_2 nanoparticles (MNPs) with a typical diameter less than 20 nm (Fig. 4F). The growth mechanism of MnO_2 nanostructures during the ultrasonic-electrodeposition process may be a crucial topic that deserves further studies. In this work, the mass of the MnO_2 deposited on the IL-GP is determined from the weight difference between the electrode before and after electrodeposition by a high-precision microbalance. The specific deposit mass is controlled to be almost equal for MNNs, MFW and MNPs depending on the electrodeposition cycles and time.

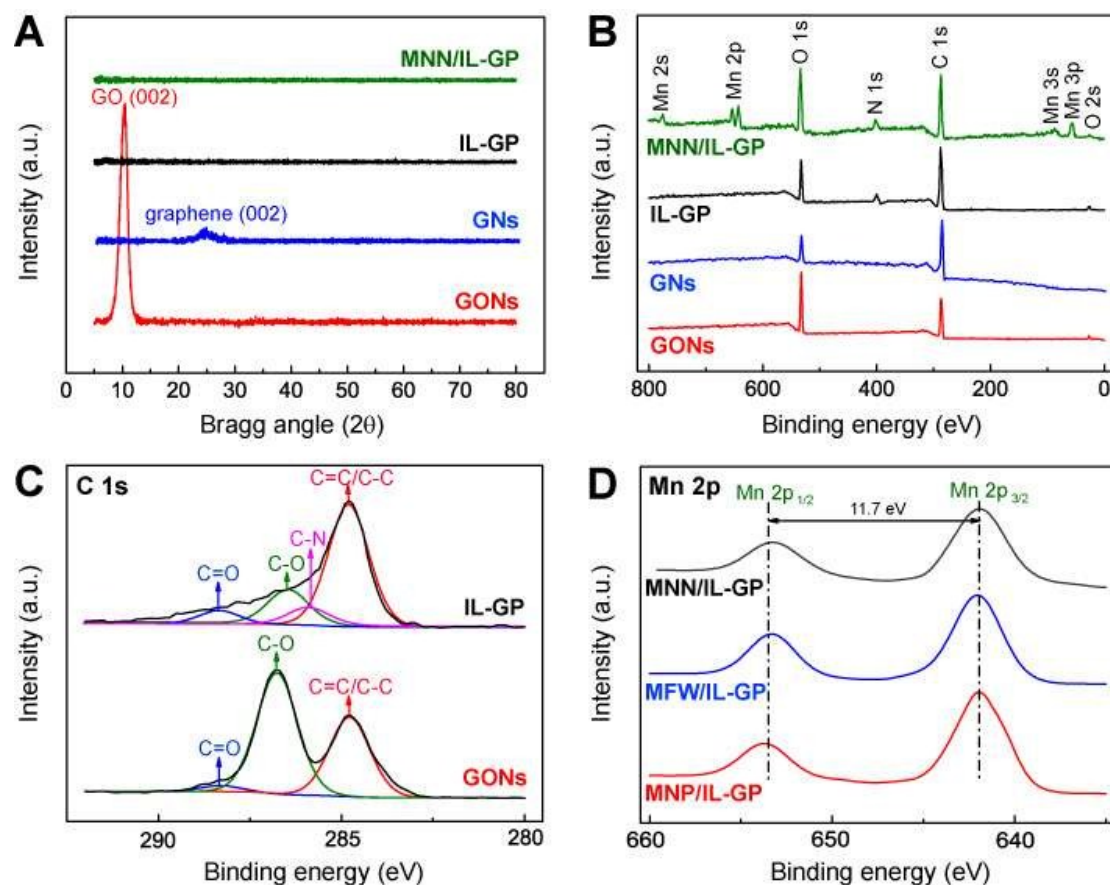


Fig. 5 (A) XRD patterns and (B) XPS survey spectra of GONs, GNs, IL-GP and MNN/IL-GP samples. (C) Curve fit of C 1s spectra of GONs and IL-GP samples. (D) Curve fit of Mn 2p spectra of MNN/IL-GP, MFW/IL-GP and MNP/IL-GP samples.

The typical X-ray diffraction (XRD) patterns of the GONs, GNs, IL-GP and MNN/IL-GP are shown in Fig. 5A. For GONs sample, the sharp peak at about $2\theta = 10.4^\circ$ corresponds to the (002) reflection of stacked GONs, suggestive of the presence of oxygen-containing groups on GONs. After chemical reduction by hydrazine, the sharp peak assigning to the (002) reflection of stacked GONs is invisible, and a new broad peak at about $2\theta = 24.4^\circ$ can be seen from GP, confirming the elimination of the oxygen-containing groups on the GNs.⁴⁴ For IL-GP sample, the dominant peak that normally observed for graphene sample is imperceptible, indicating a highly disordered overlay of individual IL-GNs formed in the IL-GP architecture. After the electrodeposition of MNNs on IL-GP, no obvious diffraction peaks assigned as the crystal planes of MnO_2 can be observed, demonstrating the forming of amorphous nature of MnO_2 nanostructure on IL-GP. As a matter of fact, for SC application, the amorphous MnO_2 coatings on electrode is more favourable than the crystalline MnO_2 coatings due to easy penetration of ions through the bulk of the active material.^{12, 45}

The surface chemical compositions and the valence states of samples are investigated by the X-ray photoelectron spectroscopy (XPS). As shown in Fig. 5B, for the GONs sample, the main peak centered at about 285 eV originates from the graphitic sp^2 carbon atoms, and the binding energies located at 530 eV are due to oxygenate groups. A similar phenomenon is observed for GNs, however, the intensity of peaks related to oxygenate groups are much lower than that of GONs, indicative of the desirable deoxygenation by the reduction process. For IL-GP, an additional

peak corresponding to C-N and/or C=N at 400 eV is appeared, in accordance with the FTIR results. The absence of Br 3d peak between 65 and 85 eV indicates that Br anions may have been exchanged by hydroxyl anions.⁴⁶ The XPS spectrum of MNN/IL-GP illustrates that besides the C 1s, O 1s and N 1s signals from IL-GP, two characteristic peaks corresponding to Mn 2p can be observed, confirming the presence of Mn element in the composite. The curve fits of C 1s spectra of GONs and IL-GP are shown in Fig. 5C. The XPS spectrum of GONs indicates the presence of two main types of carbon bonds of C=C/C-C (284.8 eV) and C-O (286.6 eV). In the case of IL-GP, the peaks associated with C=C (284.8 eV) become predominant, while the peaks of C-O assigned to the carbon in epoxy/ether groups are greatly weakened. In addition, a new peak related to the C-N bound appears at 285.9 eV. These results taken together indicate the successful covalent functionalization of graphene with amine-terminated IL through a nucleophilic ring-opening reaction between the epoxy groups of GONs and the amine groups of an amine-terminated IL. The core-level XPS signals of Mn 2p in MNN, MFW and MNP modified IL-GP samples reveal the Mn $2p_{3/2}$ and $2p_{1/2}$ centered at 641.8 and 653.4 eV, respectively, with a spin-energy separation of 11.6 eV (Fig. 5D), indicating that the element Mn is present in the chemical state of Mn (IV) in different samples.²² From the atomic percentages of C, O and Mn, the weight ratio of MNN component in MNN/IL-GP is estimated to be ~54.1 wt%. In order to reveal the 3D distribution of MnO_2 in MNN/IL-GP, energy dispersive X-ray spectroscopy (EDX) was adopted to detect the weight ratio of MnO_2 in different location of MNN/IL-GP (Fig.

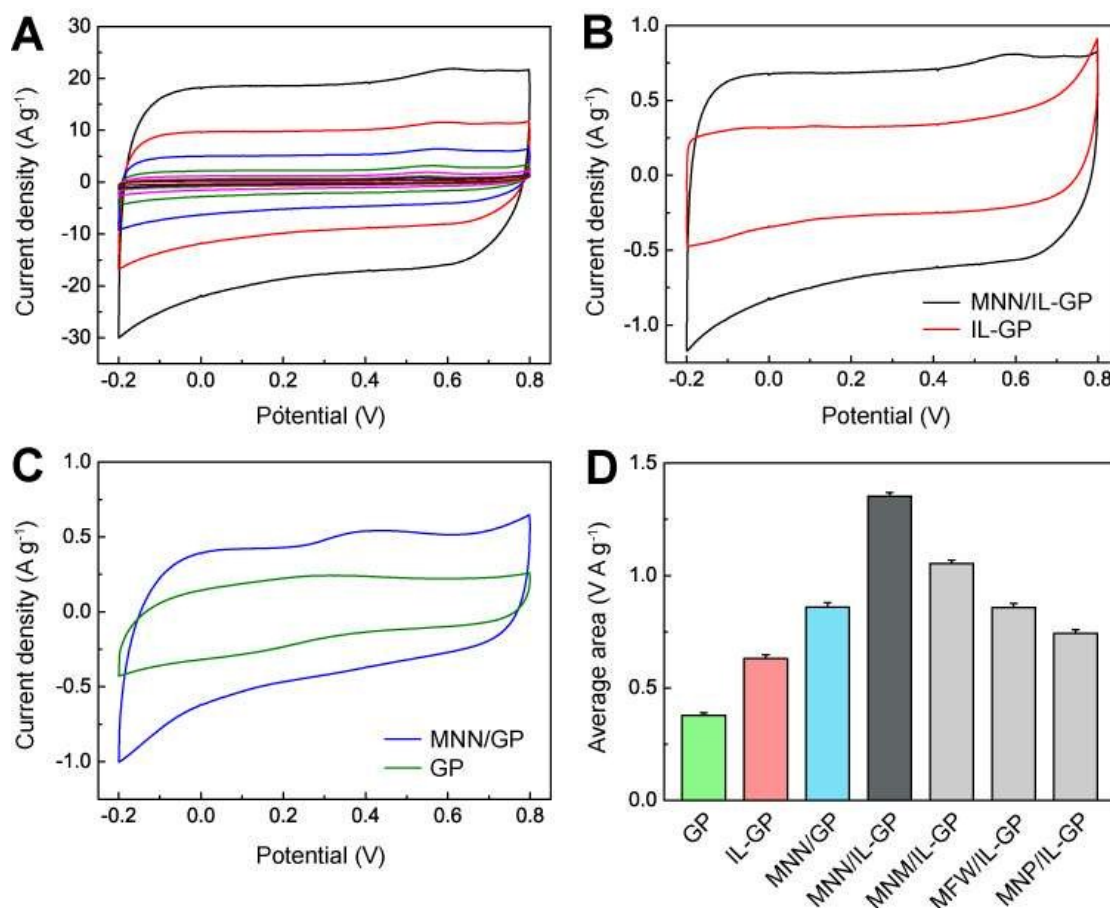


Fig. 6 (A) CV curves for MNN/IL-GP electrode at different scan rates (2, 5, 10, 20, 50, 100 and 200 mV s⁻¹ from inner to outer) in 1.0 M Na₂SO₄ electrolyte. (B) CV curves for MNN/IL-GP and IL-GP electrodes (from outer to inner) at the same scan rate of 5 mV s⁻¹. (C) CV curves for MNN/GP and GP electrodes (from outer to inner) at the same scan rate of 5 mV s⁻¹. (D) Histograms of average area of CV curves for GP, IL-GP, MNN/IL-GP, MNM/IL-GP, MFW/IL-GP, MNP/IL-GP electrodes at the same scan rate of 5 mV s⁻¹.

S1). The measurable Mn signals indicate MnO₂ exist in both exterior and interior part of MNN/IL-GP, suggesting that MNNs not only grow on paper surface but also penetrate into the layer of IL-GP during the *in situ* electrodeposition. The weight ratio of MnO₂ in the exterior region is ~32.5 wt%, which is higher than that in the interior region (~19.6 wt%), revealing that MNNs is trend to grow on the exterior part of IL-GP. The systematic difference obtained from XPS and EDX is because EDX characterizes the entire sample, whereas XPS probes a thin surface layer. Such inhomogeneous distribution of MnO₂ in IL-GP can also be observed for MNM/IL-GP, MFW/IL-GP and MNP/IL-GP samples.

Electrochemical performance of the nanohybrid paper SC

The supercapacitive activity of different nanohybrid paper electrodes has been tested in three-electrode system using them as the working electrodes. The cyclic voltammetry (CV) curves of MNN/IL-GP electrode at different scan rates are carried out with potential windows ranging from -0.2 to 0.8 V in 1.0 M Na₂SO₄ aqueous electrolyte solution. As shown in Fig. 6A, the CV curves of MNN/IL-GP show the rectangular and symmetric shape even at the scan rate of 200 mV s⁻¹, indicative of perfect electrical double-layer capacitance behaviour and fast charging/discharging process characteristic.⁴⁷ To explore the advantages of MNN/IL-GP as an ideal electrochemical capacitive electrode, we have investigated its

CV response with controllable IL-GP, MNN/GP and GP carried out at different scan rates (2, 5, 10, 20, 50, 100 and 200 mV s⁻¹) in 1.0 M aqueous Na₂SO₄ electrolyte (Fig. S2). The results reveal that both MNN/IL-GP and MNN/GP exhibit better electrochemical capacitive characteristics and superior reversible redox reaction than IL-GP and GP due to the double layer contribution along with the pseudocapacitive contribution (Fig. 6B and 6C). Furthermore, the comparison between IL-GP and GP displays that although the CV curves of both IL-GP and GP show quasi-rectangular shape, the leveled current separation between leveled anodic and cathodic currents for GP is much smaller. Moreover, a pair of redox peaks for GP sample is visible, which assign to the transition between quinone/hydroquinone groups on carbon-based materials.

The electrochemical properties of the overall system of SCs are mainly estimated by specific capacitance (C_s). Since C_s is proportional to the average areas of CVs, in this work, the integration over the full range of CV curves of MnO₂ with different morphologies of MNN, MNM, MFW and MNP is conducted to determine the average value. The results indicate the average areas of these samples quantitatively change in the following order: MNN/IL-GP > MNM/IL-GP > MFW/IL-GP > MNP/IL-GP (Fig. 6D). Among all nanostructured MnO₂, MNN/IL-GP has highest C_s value and therefore are expected to realize many practical

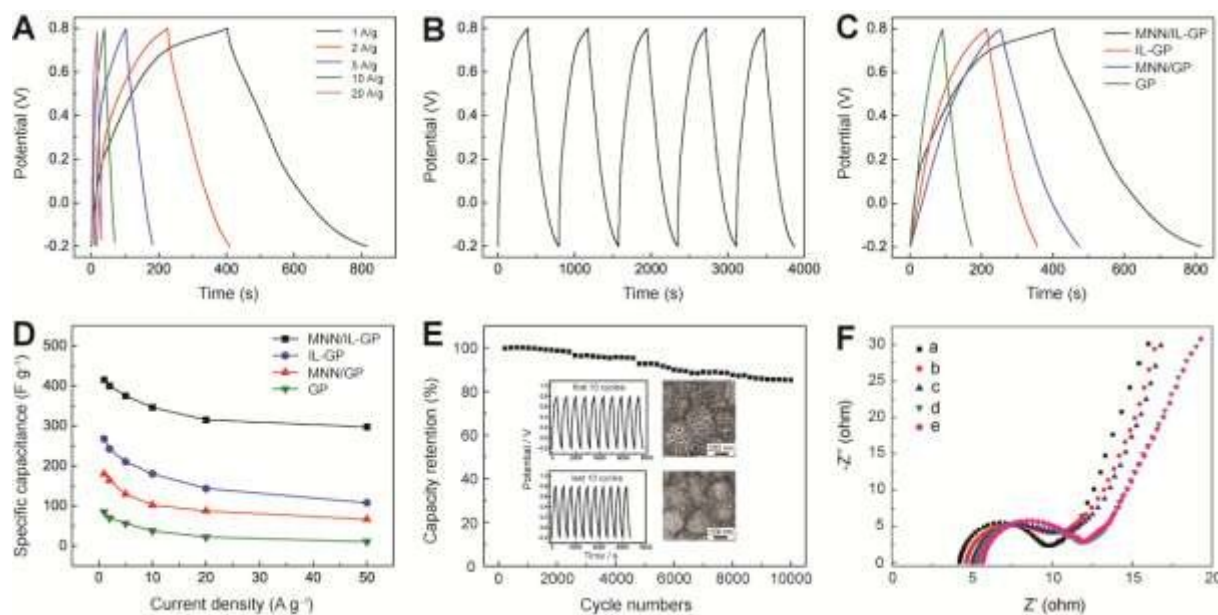


Fig. 7 (A) GV charge-discharge measurement of MNN/IL-GP electrode at different current densities (1~20 A g⁻¹, from right to left). (B) GV charge-discharge measurement of MNN/IL-GP electrode at the current density of 1 A g⁻¹. (C) Specific capacitances of MNN/IL-GP, IL-GP, MNN/GP and GP electrodes (from right to left) at the same current densities of 1 A g⁻¹ derived from GV charging/discharging curves. (D) The capacitance retention ratio of MNN/IL-GP, IL-GP, MNN/GP and GP (from top to bottom) as a function of discharge current densities. (E) Charge/discharge cycling test at the current density of 5 A g⁻¹. Inset shows the GV charge/discharge cyclic curves of the first and last 10 cycles, and SEM images of MNNs/IL-GP before (top) and after (bottom) after 10000 cycles. (F) EIS curves of MNN/IL-GP electrode after folding for 0 (a), 100 (b), 200 (c), 500 (d) times and under the folding state (e).

applications that require large capacitance and high energy storage.^{48,49} As reported by Devaraj et al., two factors are thought to make contribution to the high C_s , those are the high specific area of nanoscale MnO₂ and good alignment of nanostructure that can provide well-ordered tunnels, convenient for insertion/extraction of electrolyte ions into/from MnO₂.⁵⁰ By definition, MnO₂-based electrode involves redox reactions in CV tests as the Mn atoms in the overlayer are converted into higher/lower valence states. Based on this, the pseudocapacitance is conspicuously dependent on the effective surface area of nanostructured MnO₂.⁵¹ In this work, although both MNNs and MNM consist 3D network structure of MnO₂ nanowire, MNNs possess higher weight ratio of MnO₂ and hence provide larger surface area of electrode in contact with the electrolyte than MNM. On the other hand, the morphology also has significant influence on the C_s of MnO₂. Even though the mass of the MnO₂ are almost equal for MNNs, MFW and MNPs on the IL-GP, the MNPs results in only a very thick top layer (up to a few hundreds of nanometers) and/or densely packed nanostructure of MnO₂ participating in the charge storage process, leading to an increased electrode resistance and a decreased C_s due to the low proton diffusion constant and electrical conductivity of MnO₂ materials. In contrast, MNNs and MFW possess a mesoporous structure from the interlocked nanowires or nanoflakes architecture and pores exist among the nanowires and nanoflakes, which enable effective electrolyte ion transport during SC operations. Additionally, given the higher C_s value of IL-GP than that of GP, we suppose that IL-GP with larger specific surface area has provided more conductive channels to facilitate the access of the aqueous electrolyte ions onto the graphene surface.

To get more information about the potential of as-prepared MNN/IL-GP as electrode materials for SCs, the constant-current galvanostatic (GV) charge/discharge curves of the MNN/IL-GP at

different current densities are illustrated in Fig. 7A. During the charging and discharging steps, the charge curves of MNN/IL-GP are almost symmetric to its corresponding discharge counterpart and can even be maintained at a low density of 1 A g⁻¹ (Fig. 7B). The C_s for different electrodes with an increase in current density is shown in Fig. 7C and 7D, which is calculated on the basis of the charge/discharge curve.⁵² MNN/IL-GP exhibits the higher C_s values with respect to MNN/GP, IL-GP and GP. Meanwhile, its C_s preserves 76 % (from 415 to 315 F g⁻¹) as the current densities increase from 1 to 20 A g⁻¹. However, the C_s of MNN/GP are not only much lower than the ternary composite but also decrease significantly with increased current densities (e.g., from 268 to 143 F g⁻¹ at current density of 1~20 A g⁻¹). Similar results are observed in IL-GP (e.g., from 180 to 87 F g⁻¹ at current density of 1~20 A g⁻¹) and GP (e.g., from 85 to 22 F g⁻¹ at current density of 1~20 A g⁻¹) as well. Furthermore, the comparison between different nanostructured MnO₂ decorated IL-GP also indicates that the maximum value of C_s for MNN/IL-GP (415 F g⁻¹) is much higher than that of MNM/IL-GP (321 F g⁻¹), MFW/IL-GP (256 F g⁻¹) and MNP/IL-GP (218 F g⁻¹) in this work. The detailed information has been shown in Supporting Information (Table S1). And the maximum value of C_s for MNN/IL-GP is also more competitive than MnO₂ with other morphologies, such as MnO₂ nanoflower (315 F g⁻¹),⁵³ MnO₂ nanorods (302 F g⁻¹),⁵⁴ MnO₂ nanolamellas (206 F g⁻¹),⁵⁵ MnO₂ hollow urchins (147 F g⁻¹)⁵⁶ and MnO₂ clews (120 F g⁻¹)⁵⁷ reported previously. The high C_s as well as superior rate capability in the MNN/IL-GP electrode can be attributed to the synergetic contribution from MNNs, ILs and GP ternary nanostructure, which can be recognized as: i) the IL-GP possesses large surface area and open interlayer spacing, allowing effective loading of MnO₂ and facilitating easy access of electrolyte ions to electrode surfaces; ii) MnO₂ nanomaterials are directly grown on conductive IL-GP by *in-*

situ ultrasonic-electrodeposition. This provides an excellent interfacial contact between MnO₂ and IL-GP electrode for fast electron transport, resulting in small contact resistance and high rate performance; (iii) Porous MNN architecture that interweaved from individual MnO₂ nanowires provides large electrochemically active surface area for charge transfer and reduces ion diffusion length during the charge/discharge process, which is helpful for high-power applications when the capacitor is charged or discharged at high current density; iv) MNN/IL-GP electrode exhibits remarkably enhanced electrochemical capacitance by synergetic combining the electric double-layer capacitance of IL-GP and Faradaic pseudocapacitance of MnO₂.

The cycle stability is a crucial parameter in SCs operations. However, the cycle life of pseudocapacitive materials such as metal oxides or conducting polymers is limited because of the structure or volume changes during redox reactions leads to the loss of active materials.²⁴ Our design of the incorporation of pseudocapacitive MnO₂ into graphene-based paper material effectively improves the cycle performance of the resultant electrode. In this study, the cycle stability of MNN/IL-GP composite has been tested by repeating GV test in the voltage window from -0.2 to 0.8 V at a current density of 10 A g⁻¹. The as-prepared electrochemical capacitor shows ~85% capacitance retention over 10000 cycles (Fig. 7E). The charge-discharge curves of last 10 cycles remain almost the same shape with the first 10 cycles. Moreover, the SEM images reveal that the whole structural integrity of MNNs on the IL-GP is well maintained after 10000 cycles (Fig. 7E inset). This is because the MNNs are *in situ* grown on IL-GP rather than mechanical blending. Furthermore, the conductive IL-GP not only serves as a substrate to immobilize MNNs and keep them bound together during the cycling tests, but also functionalizes itself by imparting better transporting to the hybrid electrode, which consequently improve the electrochemical properties and cycling stability of the resultant SC electrode.

To study the mechanical stability of the resultant paper electrodes in harsh environment such as folding/twisting conditions, we have investigated the effects of the bending-induced mechanical stress on the electrochemical performance of flexible MNN/IL-GP electrode. Fig. 7F displays the electrochemical impedance spectra (EIS) of MNN/IL-GP after repetitive folding and under the folded state. The EIS of MNN/IL-GP electrode exhibits a small semicircle over the high frequency range, followed by a linear part in the low frequency region. Notably that the small semicircle indicates a low interfacial charge-transfer resistance, whereas ideally polarizable capacitance gives rise to a straight vertical line along the series.⁵⁸ It can be seen from the Nyquist plots that the equivalent series resistances (R_{ESR}) is ~5 Ω calculated from the x-intercept on the plot and the semicircle is quite small. Moreover, MNN/IL-GP has quite straight line in the low frequency region due to a lowered diffusion resistance by the shortened proton diffusion path. After repetitive folding for 500 times or under the folded state, only a subtle change can be observed in the overall resistance behavior, which demonstrates the exceptional electrochemical stability of the SC electrode.

Conclusions

In summary, we have demonstrated the fabrication of a new type of sandwich-structured nanohybrid paper based on controllable growth of nanostructured MnO₂ on free-standing IL-GP *via* template-free ultrasonic-electrodeposition approach, and explored its practical application as flexible electrode for SC application. The as-obtained nanohybrid electrode inherited the unique pseudocapacity of metal oxide, the high conductivity and electric double layer charging/discharging of IL-graphene composite, and the distinguished mechanical stability, and therefore exhibited good supercapacitive properties in terms of high specific capacitance,

excellent rate capability, good cycling stability and ultimate flexibility for device packaging. We envision that our modular approach for designing sandwich-structured nanohybrid paper electrodes with tailored structure properties can be generalized toward other functionalized graphene paper materials modified by a diverse group of pseudocapacitive materials such as RuO₂, SnO₂, NiO and Co₃O₄ and their alloy, offering new insights on designing various nanohybrid paper electrodes to realize high-energy density and high-power density characteristics for their potential applications in advanced flexible and lightweight electrochemical capacitor devices.

Acknowledgements

This work is supported by the National Natural Science Foundation of China (Grant 50773059) and the program of Nanyang Assistant Professorship of Nanyang Technological University, Singapore.

Notes and references

^a School of Material Science and Engineering, Wuhan Institute of Technology, Wuhan, Hubei 430073, People's Republic of China *E-mail: ymsun1982@hotmail.com

^b School of Chemical and Biomedical Engineering, Nanyang Technological University, 70 Nanyang Drive 637457, Singapore *E-mail: hduan@ntu.edu.sg

Electronic Supplementary Information (ESI) available: EDX spectra of inner part and exterior part of MNN/IL-GP, the weight ratio of MnO₂ for MNN/IL-GP, MNM/IL-GP, MFW/IL-GP and MNP/IL-GP electrodes estimated from EDX analysis; CV curves of MNN/IL-GP, IL-GP, MNN/GP and GP at different scan rates; Integrated area of CV curves and C_s derived from GV charging/discharging curves of different electrodes, See DOI: 10.1039/b000000x/

- X. M. Lu and Y. N. Xia, *Nat. Nanotechnol.*, 2006, **1**, 163.
- Z. Ling, C. E. Ren, M.-Q. Zhao, J. Yang, J. M. Giammarco, J. Qiu, M. W. Barsoum and Y. Gogotsi, *Proc. Natl. Acad. Sci. U. S. A.*, 2014, **111**, 16676.
- Y. He, W. Chen, C. Gao, J. Zhou, X. Li, and E. Xie, *Nanoscale*, 2013, **5**, 8799.
- Y. He, W. Chen, X. Li, Z. Zhang, J. Fu, C. Zhao and E. Xie, *ACS Nano*, 2013, **7**, 174.
- L. Yuan, X. H. Lu, X. Xiao, T. Zhai, J. Dai, F. Zhang, B. Hu, X. Wang, L. Gong, J. Chen, C. Hu and Z. L. Wang, *ACS Nano*, 2012, **6**, 656.
- Y. Cheng, S. Lu, H. Zhang, V. C. Varanasi and J. Liu, *Nano Lett.*, 2012, **12**, 4206.
- C. Yuan, L. Yang, L. Hou, J. Li, Y. Sun, X. Zhang, L. Shen, X. Lu, S. Xiong and X. W. Lou, *Adv. Funct. Mater.*, 2012, **22**, 2560.
- L. B. Hu, M. Pasta, F. La Mantia, L. F. Cui, S. Jeong, H. D. Deshazer, J. W. Choi, S. M. Han and Y. Cui, *Nano Lett.*, 2010, **10**, 708.
- L. B. Hu, J. W. Choi, Y. Yang, S. Jeong, F. La Mantia, L. F. Cui and Y. Cui, *Proc. Natl. Acad. Sci. U. S. A.*, 2009, **106**, 21490.
- J. Xiao, L. Wan, S. Yang, F. Xiao and S. Wang, *Nano Lett.*, 2014, **14**, 831.
- L. Bao, J. Zang and X. Li, *Nano Lett.*, 2011, **11**, 1215.
- R. Mas-Ballesté, C. Gómez-Navarro, J. Gómez-Herrero and F. Zamora, *Nanoscale*, 2011, **3**, 20.
- L. Gao, G. Ni, Y. Liu, A. H. Castro-Neto and K. P. Loh, *Nature*, 2014, **505**, 190.
- D. A. Dikin, S. Stankovich, E. J. Zimney, R. D. Piner, G. H. B. Dommett, G. Evmenenko, S. T. Nguyen and R. S. Ruoff, *Nature*, 2007, **448**, 457.

- 16 Y. X. Xu, H. Bai, G. W. Lu, C. Li and G. Q. Shi, *J. Am. Chem. Soc.*, 2008, **130**, 5856.
- 17 K. Chen, F. Liu, D. Xue and S. Komarneni, *Nanoscale*, 2015, **7**, 432.
- 18 S. K. Li, Y. X. Yan, J. L. Wang and S. H. Yu, *Nanoscale*, 2013, **5**, 12616.
- 19 P. Šimek, Z. Sofer, O. Jankovský, D. Sedmidubský and M. Pumera, *Adv. Funct. Mater.*, 2014, **24**, 4878.
- 20 K. Chi, Z. Zhang, J. Xi, Y. Huang, F. Xiao, S. Wang and Y. Liu, *ACS Appl. Mater. Interfaces*, 2014, **6**, 16312.
- 21 Y. Sun, K. He, Z. Zhang, A. Zhou and H. Duan, *Biosens Bioelectron.*, 2015, **68**, 358.
- 22 Z. S. Wu, W. Ren, D. W. Wang, F. Li, B. Liu and H. M. Cheng, *ACS Nano*, 2010, **4**, 5835.
- 23 Y. Sun, Q. Wu and G. Shi, *Energy Environ. Sci.*, 2011, **4**, 1113.
- 24 P. Simon and Y. Gogotsi, *Nat. Mater.*, 2008, **7**, 845.
- 25 M. M. Hantel, T. Kaspar, R. Nesper, A. Wokaun and R. Kötz, *Electrochem. Commun.*, 2011, **13**, 90.
- 26 H. Gao, F. Xiao, C. B. Ching and H. Duan, *ACS Appl. Mater. Interfaces*, 2012, **4**, 7020.
- 27 S. Ernst, S. E. Norman, C. Hardacre and R. G. Compton, *Phys. Chem. Chem. Phys.*, 2014, **16**, 4478.
- 28 T. Y. Kim, H. W. Lee, M. Stoller, D. R. Dreyer, C. W. Bielawski, R. S. Ruoff and K. S. Suh, *ACS Nano*, 2011, **5**, 436.
- 29 T. Li, N. Li, J. Liu, K. Cai, M. F. Foda, X. Lei and H. Han, *Nanoscale*, 2015, **7**, 659.
- 30 M. Armand, F. Endres, D. R. MacFarlane, H. Ohno and B. Scrosati, *Nat. Mater.*, 2009, **8**, 621.
- 31 H. Yang, C. Shan, F. Li, D. Han, Q. Zhang and L. Niu, *Chem. Commun.*, 2009, 3880.
- 32 T. Y. Kim, H. W. Lee, J. E. Kim and K. S. Suh, *ACS Nano*, 2010, **4**, 1612.
- 33 Y. Sun, Y. Cheng, K. He, A. Zhou and H. Duan, *RSC Adv*, 2015, **5**, 10178.
- 34 W. Liu, C. Lu, X. Wang, R. Y. Tay and B. K. Tay, *ACS Nano*, 2015, **9**, 1528.
- 35 F. Xiao, F. Zhao, Y. Zhang, G. Guo and B. Zeng, *J. Phys. Chem. C*, 2009, **113**, 849.
- 36 Z. Zhang, F. Xiao, L. Qian, J. Xiao, S. Wang and Y. Liu, *Adv. Energy Mater.*, 2014, 1400064.
- 37 H. S. Ahn and A. J. Bard, *J. Am. Chem. Soc.*, 2014, **136**, 14011.
- 38 Y. Lu, Z. Tu and L. A. Archer, *Nat. Mater.*, 2014, **13**, 961.
- 39 W. S. Hummers and R. E. Offeman, *J. Am. Chem. Soc.*, 1958, **80**, 1339.
- 40 Y. J. Zhang, Y. F. Shen, J. H. Yuan, D. X. Han, Z. J. Wang, Q. X. Zhang and L. Niu, *Angew. Chem. Int. Ed.*, 2006, **45**, 5867.
- 41 E. D. Bates, R. D. Mayton, I. Ntai and J. H. Davis, *J. Am. Chem. Soc.*, 2002, **124**, 926.
- 42 J. Wang, H. Chu and Y. Li, *ACS Nano*, 2008, **2**, 2540.
- 43 M. T. Lee, J. K. Chang, Y. T. Hsieh, W. T. Tsai and C. K. Lin, *J. Solid State Electrochem.*, 2010, **14**, 1697.
- 44 H. K. Jeong, Y. P. Lee, R. J. W. E. Lahaye, M. H. Park, K. H. An, I. J. Kim, C. W. Yang, C. Y. Park, R. S. Ruoff and Y. H. Lee, *J. Am. Chem. Soc.*, 2008, **130**, 1362.
- 45 S. B. Ma, K. Y. Ahn, E. S. Lee, K. H. Oh and K. B. Kim, *Carbon*, 2007, **45**, 375.
- 46 C. Vallés, C. Drummond, H. Saadaoui, C. A. Furtado, M. He, O. Roubeau, L. Ortolani, M. Monthieux and A. Pénicaud, *J. Am. Chem. Soc.*, 2008, **130**, 15802.
- 47 M. D. Stoller, S. Park, Y. Zhu, J. An and R. S. Ruoff, *Nano Lett.*, 2008, **8**, 3498.
- 48 D. Bélanger, T. Brousse and J. W. Long, *Electrochem. Soc. Interfaces*, 2008, **17**, 49.
- 49 G. Yu, L. Hu, N. Liu, H. Wang, M. Vosgueritchian, Y. Yang, Y. Cui and Z. Bao, *Nano Lett.*, 2011, **11**, 4438.
- 50 S. Devaraj and N. Munichandraiah, *J. Phys. Chem. C*, 2008, **112**, 4406.
- 51 M. Toupin, T. Brousse and D. Bélanger, *Chem. Mater.*, 2002, **14**, 3946.
- 52 J. Zhang, J. Jiang and X. S. Zhao, *J. Phys. Chem. C*, 2011, **115**, 6448.
- 53 G. Yu, L. Hu, M. Vosgueritchian, H. Wang, X. Xie, J. R. McDonough, X. Cui, Y. Cui and Z. Bao, *Nano Lett.*, 2011, **11**, 2905.
- 54 L. Yuan, X. H. Lu, X. Xiao, T. Zhai, J. Dai, F. Zhang, B. Hu, X. Wang, L. Gong, J. Chen, C. Hu, Y. Tong, J. Zhou and Z. L. Wang, *ACS Nano*, 2012, **6**, 656.
- 55 S. Chen, J. Zhu and X. Wang, *ACS Nano*, 2010, **4**, 6212.
- 56 M. Xu, L. Kong, W. Zhou and H. Li, *J. Phys. Chem. C*, 2007, **111**, 19141.
- 57 P. Yu, X. Zhang, D. Wang, L. Wang and Y. Ma, *Cryst. Growth Des.*, 2009, **9**, 528.
- 58 V. Subramanian, H. Zhu, R. Vajtai, P. M. Ajayan and B. Wei, *J. Phys. Chem. B*, 2005, **109**, 20207.